Journal of Power Sources 695 (2026) 241282

Contents lists available at ScienceDirect

Journal of Power Sources

journal homepage: www.elsevier.com/locate/jpowsour

Long-range dipole–dipole interactions governing alkali-metal adsorption and clustering on graphitic surfaces

Jafar Azizi [a,*], Axel Gross [a], Holger Euchner [b]

[a] Institute of Theoretical Chemistry, Ulm University, Germany
[b] Institute of Physical and Theoretical Chemistry, University of Tübingen, Germany

HIGHLIGHTS

- Long-range dipole interactions govern alkali adsorption on graphite.
- Surface coverage controls Li, Na, and K adsorption energetics.
- Defects strengthen adsorption and alter aggregation pathways.
- Li and Na form 3D clusters, whereas K favors layer-by-layer growth.
- Non-local effects are essential for hard-carbon anode modeling.

GRAPHICAL ABSTRACT

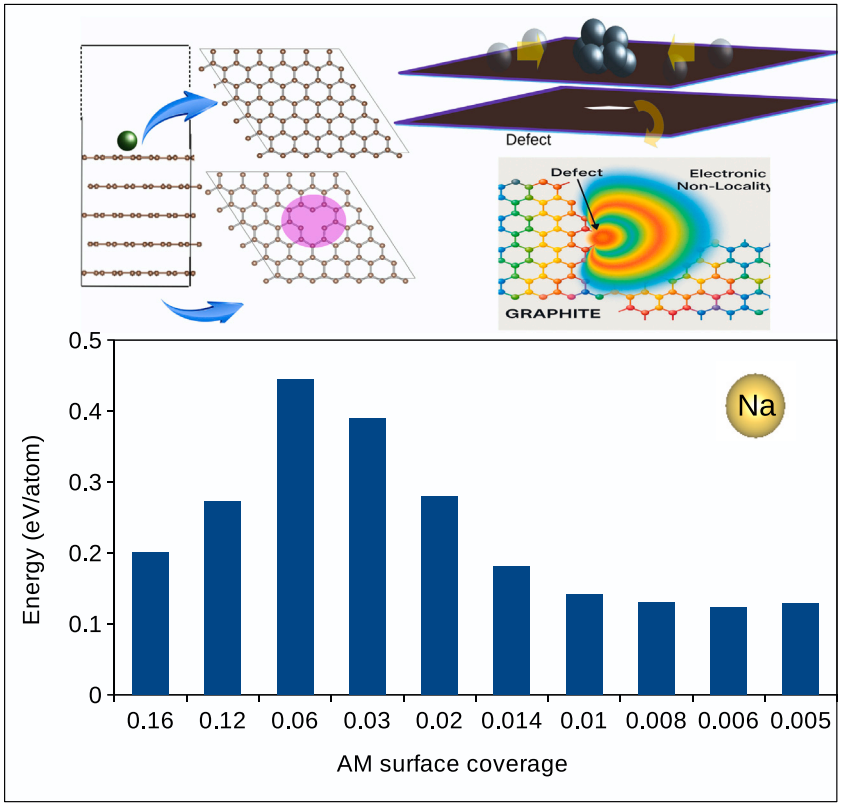

ARTICLE INFO

Keywords:
Hard carbon
Alkali-metal adsorption

ABSTRACT

Adsorption of alkali-metal atoms on graphitic surfaces plays a fundamental role in electrochemical energy storage, particularly in carbon-based anodes such as hard carbon. Using first-principles calculations, we systematically investigate alkali-metal adsorption on graphite as a function of surface coverage and demonstrate

* Corresponding author.
E-mail address: jafar-1.azizi-shoushbolaghi@uni-ulm.de (J. Azizi).

https://doi.org/10.1016/j.jpowsour.2026.241282
Received 1 June 2026; Received in revised form 17 July 2026; Accepted 15 August 2026
Available online 1 September 2026

Electrostatic interactions
Coverage dependence
Long-range dipole–dipole interactions
Aggregation

that the adsorption energetics are governed by long-range dipole–dipole interactions between neighboring atoms. In the context of hard carbon, alkali-metal clustering on graphitic surfaces constitutes a critical initial step in the filling of micro- and nanopores. We reveal pronounced differences in the energetics and growth mechanisms of Li, Na, and K clusters and show that structural defects strongly modulate clustering and stability by providing preferential adsorption sites that alter aggregation behavior. Importantly, neglecting these long-range dipole–dipole interactions, and thus the associated surface-coverage dependence, leads to a systematic overestimation of adsorption energies and an incomplete description of alkali-metal storage in carbon-based anodes. Overall, this work provides a unified physical description of coverage-dependent, long-range dipole–dipole interactions, revealing the atomic-scale mechanisms governing adsorption energetics and high-concentration clustering in graphitic carbon, along with their implications for alkali-metal storage in carbon-based anodes.

1. Introduction

The distinctive mechanical and electronic properties of graphite and its derivatives enable a broad spectrum of technological applications, including energy storage, sensors, and electronics [1–4]. Moreover, graphite-based materials play essential roles in several branches of chemistry, particularly electrochemistry and catalysis [4–8], which is based on the fact that these materials originate from diverse sources and exhibit a wide range of structural forms. In the context of energy storage, graphite and related carbon materials serve as key electrode components in supercapacitors [9–11], Li-ion batteries [12–14], and emerging post–Li-ion battery systems [15–24]. As an anode material, Li metal shows the highest possible capacity; however, Li-metal batteries are plagued by dendrite growth [25]. Therefore, graphite, which reduces the tendency for harmful dendrite formation, is typically used. Yet, for Na-ion batteries, graphite cannot be used as an anode material, as the insertion of Na into graphite is energetically less favorable than the formation of metallic Na [23]. As an alternative, hard carbon has become the material of choice for Na-ion batteries. However, the Na insertion mechanism in hard carbon remains under active debate. [26,27]. Still, there is a growing consensus that the so-called card house model and modifications thereof [28,29] faithfully describe the Na insertion mechanism. According to this model [28–30], sodium is first inserted into nearly parallel graphitic layers, preferentially at defect sites, followed by the adsorption of Na into hard carbon nanopores, eventually filling these nanopores with metal-like Na clusters. For this mechanism, the adsorption of Na on the basal planes of graphitic nanoparticles represents the initial step of the filling of the nanopores, followed by the creation of adsorbed clusters and then, eventually, metal-like clusters. Hence, cluster formation on graphitic surfaces constitutes a critical step in the proposed card house model. Nevertheless, despite its fundamental importance, the underlying mechanisms of this cluster formation process remain insufficiently explored. In addition, the investigation of processes at electrode surfaces is of particular interest due to their critical influence on the battery performance. First, adsorption accounts for a considerable portion of the alkali-metal storage capacity in graphite-derived electrodes, particularly in hard carbon with its enlarged surface area [26,31]. Second, the complex nature of alkali metal (AM) bonding to graphite has become a central topic for explaining experimental observations with respect to the AM intercalation [32,33]. A detailed understanding of AM–graphite interactions and adsorption mechanisms is therefore crucial for guiding the design and optimization of next-generation anode materials. Despite the electronic simplicity of alkali metals, the nature of their interaction with graphite – especially the coverage dependence of adsorption energetics – remains debated [34]. Density functional theory (DFT) has been the principal tool for theoretical studies of these systems, offering reliable insights into electronic structure and energetics [35–41]. However, DFT may systematically overemphasize ionic interactions, thereby influencing the predicted bonding characteristics and adsorption trends [34,42–45]. The charge transfer during AM adsorption on graphitic surfaces results in changes of the electronic states of substrate and AM atoms, which consequently highly affects the adsorption process at different surface coverages. Finally, the adsorption of the AM atoms affects the graphite surface geometry, which again may affect the adsorption process [46–50]. It is worth noting that systematic investigations, exploring the adsorption energy trends of Li, Na, and K as a function of surface coverage, are scarce in the literature [51,52]. Existing reports on Li suggest that higher coverages further destabilize Li adsorption. Experimentally, AM adsorption can, for example, be studied by high-resolution low-energy electron diffraction (HR-LEED) and by electron energy loss spectroscopy (EELS). Li et al. combined both techniques [53,54]. Their EELS spectra show a plasmon peak for AM concentration below 0.1 ML, which changes with increasing coverage and thereafter disappears when more AM atoms are adsorbed. In fact, the change from an AM-dispersed phase to the development of close-packed islands is correlated with the concentration at which the plasmon mode stops shifting and begins to fade away [54–58]. Ultimately, the inherently amorphous structure of hard carbon underscores the importance of examining how defects influence electrochemical energy storage performance. Defects often exhibit non-local effects, meaning their influence is not confined to the immediate atomic site at which they occur. Rather, the presence of a defect can perturb the electronic structure, charge distribution, and lattice configuration over a broader region of the material. In this work, we employ first-principles based calculations to systematically investigate the adsorption behavior of Li, Na, and K atoms on graphitic surfaces over a broad range of coverages. We demonstrate that increasing coverage induces a transition from isolated adsorption to cooperative interactions that promote cluster formation, accompanied by pronounced changes in adsorption energetics and charge redistribution. Our results reveal that adsorbate concentration strongly influences adsorption energies, thereby governing both the structural and thermodynamic stability of the adsorption process. Moreover, by explicitly accounting for the non-local effects of structural defects on adsorption energetics, we provide a more comprehensive description of cluster formation under realistic conditions, where defect densities are typically high.

2. Computational methods

Periodic DFT has been used to investigate AM adsorption on two-layer based graphitic surfaces of different lateral sizes. The considered model systems have been built as stacks of graphitic layers with a large vacuum of ≈36 Å on top of the system. Various supercells of increasing lateral size ($AMC_{N\times N\times 2}$, N=2,…,10, and 15, AM=Li, Na, K) have been constructed to examine the impact of the system size on the adsorption energy. Surface coverage was controlled by varying the lateral size of the graphite supercell while keeping one alkali-metal atom adsorbed in each supercell. Increasing the supercell size decreases the surface coverage and simultaneously increases the separation between periodically repeated adsorbates. This computational strategy isolates the influence of long-range adsorbate–adsorbate interactions on the adsorption energetics without changing the local adsorption configuration, allowing the coverage dependence to be investigated independently of changes in adsorption geometry. Moreover, systems with an increased layer thickness, represented by $6\times6\times N$ supercells (where N = 2,…,5), have been computed for comparison. The Projector Augmented Wave

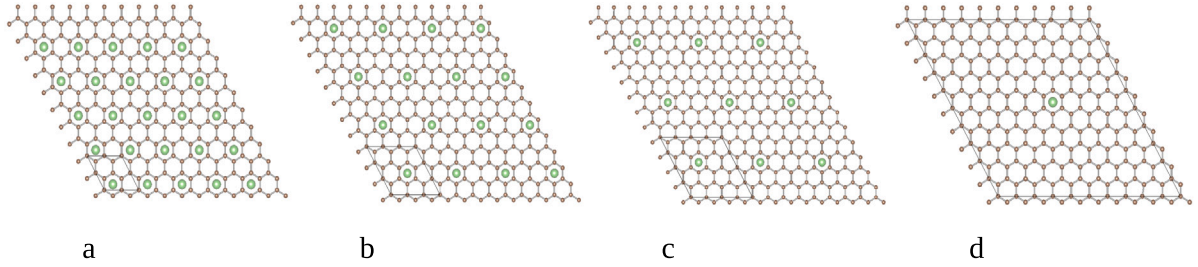

Fig. 1. AM adsorption compounds projected along the *c*-axis at surface coverages of (a) 1/8, (b) 1/18, (c) 1/32, and (d) 1/200. Simulation cells are shown in black.

(PAW) [59] approach was used and all simulations were carried out with the Vienna Ab Initio Simulation Package (VASP). Exchange and correlation were modeled using the optPBE functional, which incorporates a non-local correction scheme to account for van der Waals (vdW) interactions [60]. To assess the influence of the exchange–correlation functional on the predicted adsorption behavior, additional calculations were performed using the PBE [61] and PBE+D3 [62,63] functionals and compared with the optPBE-vdW results used throughout this work. For each functional, the lattice parameters of pristine bulk graphite were first optimized, and the resulting structural parameters are summarized in Table S1 of the Supporting Information. The electronic self-consistent field (SCF) convergence criterion was set to 10^{-7} eV, and the geometry was optimized until the residual forces were below 10^{-3} eV/Å. For all surface structures, the optimization was performed using a plane wave cutoff of 600 eV. The structures derived from the $2 \times 2 \times 2$ (corresponding to C_{16}) supercell were calculated using a $10 \times 10 \times 1$ k-point mesh, while the other examined system sizes were optimized with a corresponding k-point resolution. The convergence of the k-point sampling for the largest supercell (C400) was verified by comparing $1 \times 1 \times 1$, $2 \times 2 \times 1$, and $3 \times 3 \times 1$ k-point meshes. The selected $2 \times 2 \times 1$ mesh provides well-converged adsorption energies while maintaining computational efficiency (see Fig. S1 in the SI). Finally, to investigate AM plating on the graphite surface, a large supercell (C_{400}) was selected. For this system the convergence criterion for the SCF cycle and the residual forces during geometry optimization were reduced to 10^{-5} eV and 10^{-2} eV/Å, respectively, while a plane wave cutoff of 400 eV was applied. In addition, ab initio molecular dynamics (AIMD) simulations in the canonical ensemble at a temperature of 300 K were performed for this supercell. Using the Nosé-Hoover thermostat, each simulation was run for several picoseconds (ps) with a time step of two fs. To comprehensively investigate the aggregation and growth behavior of alkali metals on graphite, three complementary computational approaches were employed. Sequential adsorption calculations were performed to evaluate the thermodynamic evolution of adsorption during progressive cluster growth. In parallel, homogeneous initial configurations were used to identify the onset of spontaneous aggregation as a function of coverage. Finally, AIMD simulations followed by DFT relaxation were carried out to verify that the observed clustering behavior also occurs spontaneously under thermal conditions. Together, these complementary approaches provide both thermodynamic and dynamic insights into alkali-metal nucleation and growth on graphite.

3. Results and discussion

3.1. AM adsorption on pristine graphite

Given the higher energetic stability of AB-stacked graphite relative to AA stacking (by several meV per atom) [24], the substrate was modeled as a two-layer slab with AB stacking. Adsorption energies were then evaluated relative to the alkali-metal–free reference system:

$$E_{ads} = E_{G+AM} - (E_G + E_{AM}) \quad (1)$$

Here, E_{G+AM} is the total energy of the graphitic system after the AM adsorption, and E_G is the energy of the graphitic substrate, whereas E_{AM} is the energy of Li, Na, and K, respectively, in the bulk metal phase (bcc). In agreement with earlier studies, we observe that Li and Na adsorption on pristine graphite is not favorable with respect to the formation of the corresponding bulk metals [64–66]. However, our results indicate that the AM surface coverage plays a decisive role in governing the adsorption energetics. As the coverage decreases, the adsorption energy for Li and Na becomes notably more favorable, indicating a reduction in repulsive interactions, associated with an increasing distance between the adsorbates (see Figs. 1 and 2). Nevertheless, even under reduced coverage, Li and Na still exhibit positive adsorption energies, implying that their adsorption remains thermodynamically unfavorable with respect to the formation of the bulk metal. This is the correct reference in battery applications because it reflects the fact that the corresponding AM atoms would not enter the anode material but rather form bulk metal outside of the anode which leads to plating. However, we are here concerned with the details of the cluster formation process once the AM atoms have already entered the voids of the hard carbon. All positive adsorption energies shown in Fig. 2a are sufficiently small that adsorption remains energetically favorable with respect to isolated AM atoms, despite being unfavorable relative to the bulk-metal reference state used in Eq. (1). Hence, they will adsorb on the graphite plane and can then serve as nuclei for a subsequent cluster formation. Furthermore, note that also any finite isolated AM cluster in the voids will gain energy upon deposition on the graphite surface. This is due to the fact that those AM atoms that become attached to the graphite interact attractively with the carbon atoms while at the same time the energetically costly surface area of the cluster will become smaller. However, it should be emphasized again that as long as the adsorption energy of the clusters per atom is more positive than the cohesive energy of the corresponding bulk metal, the resulting structures are thermodynamically unstable with respect to plating. Furthermore, it has to be noted that in contrast to Li and Na, K demonstrates a remarkably different behavior: at low surface coverages K adsorption on graphite is energetically favorable with respect to K bulk formation, which even extends to higher coverages. This contrast highlights the inherent differences in adsorption tendencies among the considered AM species. For instance, by reducing the AM surface coverage from 1/6 to 1/200, the adsorption energy for Li, Na, and K changes from ≈ 0.53 eV, ≈ 0.20 eV, and ≈ −0.11 eV, to ≈ 0.1 eV, ≈ 0.1 eV, and ≈ −0.7 eV, respectively. With respect to the effect of AM surface coverage on the adsorption energy, this behavior can be attributed to long-range repulsive dipole–dipole interaction between the adsorbed AM atoms. In order to verify this, we determined the total charge of the adsorbed AMs. Clearly, upon adsorption, charge transfer from the AM atoms to the graphite surface occurs, as can be inferred from the corresponding charge density difference plots (see Fig. 2b), leading to the formation of dipoles. The electrostatic repulsion between these dipoles consequently increases at higher coverages, i.e., with lower distances (before cluster formation starts), leading to less favorable adsorption energetics [67]. To exemplify this point, we considered two AM atoms on the surface of a very large graphite supercell (C_{900}) and slowly increased the

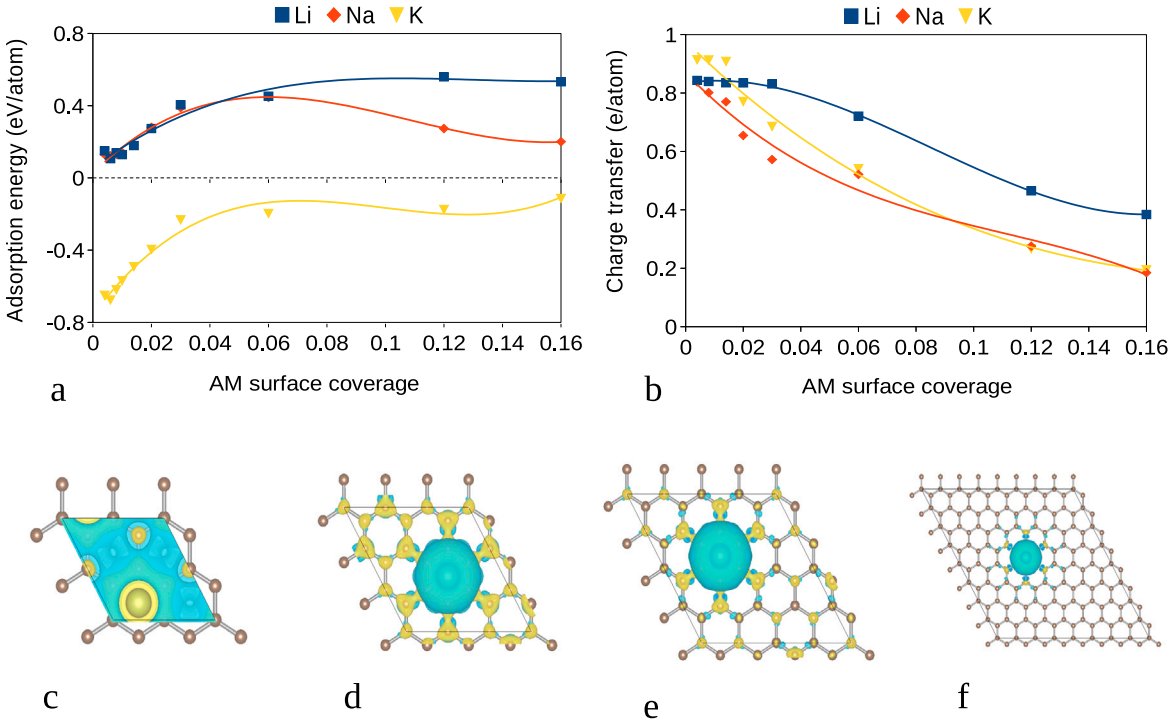

Fig. 2. Adsorption properties of Li, Na, and K on pristine graphite vs. surface coverage: (a) adsorption energy and (b) charge transfer from adsorbed AM atoms. Charge density differences for AM atoms at coverages of (c) 1/8, (d) 1/32, (e) 1/50, and (f) 1/128. Lower coverages lead to more localized charges and increased spacing between adjacent AM atoms, reducing their interaction. Surfaces plotted at 0.0009 e Å^{-3} isosurface.

AM-AM distance by moving one AM from one hexagonal site to the next. Especially for Li, the repulsion is significantly increasing as the two atoms get closer to each other (see Fig. 3). To further analyze the electrostatic interactions, planar-averaged electrostatic potential differences, $\Delta V(y)$, between the Li-containing systems (Li_2C_{900}) and pristine graphite were calculated for configurations with different Li–Li separations (see Fig. S2 in SI). The potential profiles for short and large Li–Li separations show similar distributions, with a minor energy shift of approximately 0.1 eV for the shorter Li–Li distance configuration.

A quantitative analysis of the charge transfer was achieved by examining the charge variation of the adsorbed AMs as a function of coverage (see Fig. 2b-f). In fact, at low concentrations, the charge transferred from the AM atoms to the graphite surface is obviously higher. The charges of the adsorbed AMs were determined via the DDEC6 method [68,69], showing an increasing charge transfer with decreasing surface coverage. While for Li the charge transfer quickly increases from 0.38 e to a value of 0.84 e at coverages of 1/6 and 1/200, for Na an increase from 0.18 e to 0.83 e is observed. For K, the charge transfer starts from 0.19 e and even reaches a value of 0.91 e. At increased AM surface coverage (1/6), the charge transfer from Na and K to the graphite surface is significantly decreased for Na(≈ 0.18 e) and K(≈ 0.19 e), whereas a value of 0.38 e is observed for Li. The reduced charge transfer from the AM atoms to the graphite surface at high concentration reduces the electrostatic repulsion, hence the system becomes more favorable for AM adsorption energetically (see Fig. 3). This can also be understood with respect to the formation of metallic (-like) AM clusters. The charge-density difference maps demonstrate electron depletion around the adsorbed alkali-metal atoms and electron accumulation on the graphite surface, confirming substantial charge transfer from the adsorbates to the graphite substrate and the formation of adsorption-induced interface dipoles. To provide a quantitative measure of this polarization, the effective interface dipole moments were estimated from the DDEC6 charge transfer and the equilibrium adsorption height according to μ_{eff}=q$_{DDEC}$ h. Although this represents

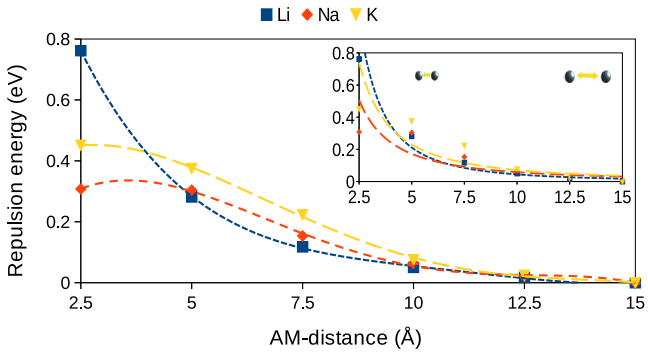

Fig. 3. Repulsion energy between two AM atoms adsorbed on graphite as a function of their separation. The system energy with the atoms at a large distance was taken as the reference.

an approximate description of the adsorption-induced interface dipole, the estimated values provide quantitative support for the existence of significant interfacial polarization, consistent with the proposed role of long-range electrostatic interactions in governing the adsorption behavior (see Table S2-7 in SI). However, still comparing the adsorption energies at high and at low coverage shows that a reduced AM surface coverage yields an enhanced adsorption strength (see Fig. 2a). While the above results show more favorable adsorption energies at low coverage, it should be noted that the corresponding diffusion barriers remain nearly unchanged across different coverages, as indicated for the case of Li (see Fig. S3 in the SI).

To ensure the reliability of this model with respect to the impact of the layer thickness, we also investigated the distance-dependent adsorption energies of the AM atoms by describing exchange and correlation via PBE and PBE+D3 (see Fig. S4 in SI). For both data sets, the same

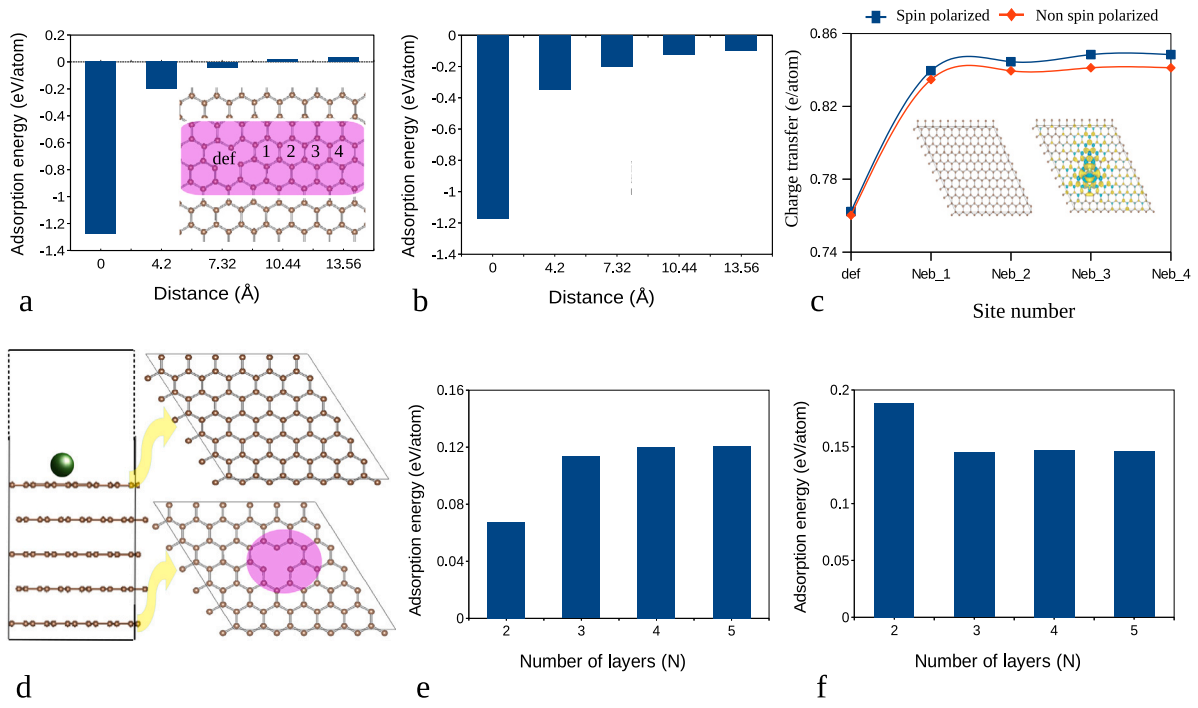

Fig. 4. Adsorption energy of Li on LiC_{400} with a MV defect (see Fig. S7 in SI) as a function of distance from the defect center for (a) non-spin-polarized and (b) spin-polarized calculations, and (c) the corresponding charge transfer from Li to the surface. Site numbering is shown in the inset of (a). Spin densities for pristine graphite (PG) and defective graphite are shown at an isosurface value of 1×10^{-4} CA^{-3} (see Fig. S8 in the SI). Panels (d–f): Li adsorption as a function of the number of graphite layers – (d,e) defect in the bottom layer and (f) pristine graphite without defects.

trend as compared to the optPBE results is obtained, only differing by the absolute values of the adsorption energy. The comparison with PBE and PBE+D3 functionals shows that the predicted adsorption trends remain consistent with those obtained using optPBE-vdW, indicating that the conclusions are not sensitive to the choice of the exchange–correlation functional. In addition to varying the coverage by changing the lateral cell size, we also examined the impact of an increasing number of stacked graphitic planes on the adsorption behavior (see Fig. 4). In two-dimensional vdW materials such as graphite, the interlayer spacing is predominantly governed by vdW interactions, making the number of layers a relevant parameter to consider. Our results show that increasing the number of layers from two to three enhances Li adsorption by more than 50 meV; however, further increasing the layer count beyond three only leads to marginal changes in adsorption energy. The reason behind this change in adsorption energy is that although the vdW interaction typically follows an r^{-6} dependence, the third layer still contributes, whereas the interaction of the adsorbed Li with the fourth and fifth layer approaches zero [62,70].

Regarding two-layer systems, energy differences between PBE+D3 and PBE calculations show that the vdW interaction also has a weak effect on the AM adsorption process (see Fig. S4 and S5 in SI). This effect becomes slightly higher at low concentration, showing that at low adsorbate concentration, the role of the vdW interaction is more pronounced. The reason behind this is that at low concentrations, the graphite surface layer around the AM atoms becomes slightly curved, resulting in a different initial adsorption mechanism compared to higher AM concentrations, in which essentially the whole layer is affected, but not only the AM adsorbed site. This phenomenon slightly affects the adsorption energy [23]. Finally, to gain further insight into the general AM adsorption behavior, we examined a four-layer aluminum (Al) model system, which consistently supports the trends observed for the graphitic structure, in particular meaning that rather large supercell sizes are needed to get fully converged adsorption energies (see Fig. S6 in SI).

3.2. Defect and long range interaction

Under operating conditions, the properties of battery materials can be largely influenced by defects. This is particularly true for strongly structured systems such as hard carbon. Therefore, we also considered the adsorption of Li atoms on defective graphite surfaces. To show how defects influence the adsorption energy, the C_{400} system was considered. This represents an extension of our previous work in which we already discussed defects and impurities on graphite, but for smaller unit cells [16,24] . Whereas the Li adsorption energy on pristine graphite (C_{400}) is unfavorable by ≈ 0.14 eV, Li bonding to a defect site is much stronger with the adsorption energy amounting to −1.28 eV on a mono-vacancy (MV) defect. The interaction becomes weaker when the Li atom is located farther away from the defect center, until it reaches an adsorption energy of 0.03 eV at the center of the fourth neighboring hexagon (see Fig. 4a). Here, it is worth noticing that at the center of the first and the second neighboring hexagon, the adsorption energy is still negative. From the third neighboring hexagonal site on, the adsorption energy gets positive, i.e., unfavorable, however, these sites are still slightly more favorable for Li adsorption as compared to the pristine graphite surface. Following structural relaxation, the carbon atoms surrounding the MV undergo an asymmetric reconstruction, resulting in C–C bond lengths ranging from approximately 1.39 to 1.50 Å in the immediate vicinity of the defect. As the distance from the defect increases, the structural distortion rapidly diminishes, and the C–C bond lengths gradually recover to the pristine graphite value of approximately 1.42 Å. An additional factor that must be considered is the role of unpaired electrons in the system. In graphite, the presence of unpaired electrons leads to spin polarization effects, particularly in defective structures. While pristine graphite exhibits a negligible magnetic behavior, extensive theoretical studies [71,72] and experimental observations of room-temperature ferromagnetism [73] have demonstrated that magnetism in graphite is closely associated with defect sites and dangling bonds. Dangling bonds in graphitic systems generate a

localized magnetic moment that can affect adsorption energetics well beyond the immediate vicinity of the defect site. This is demonstrated in Fig. 4b,c which shows that the inclusion of spin-polarization results in energetically favorable Li adsorption even rather far away from the defect site. While spin polarization significantly modifies adsorption energetics at sites far from the defect, it only leads to a slight increase in adsorption strength at the defect site itself compared with the non–spin-polarized case. This behavior can be attributed to spin-induced changes in the electronic structure and bonding interactions, which modify the adsorbate–defect interaction. Deviations from the pristine C–C bond length can be used to quantify structural distortions in defect-containing systems. In the non–spin-polarized case, the C–C bond lengths at the defect site span approximately 1.39–1.46 Å, while they gradually approach the pristine graphite value of ≈ 1.42 Å with increasing distance from the defect. In the spin-polarized case, the C–C bond lengths at the defect site range from approximately 1.37 to 1.48 Å and gradually approach the pristine graphite value of ≈ 1.42 Å with increasing distance from the defect, exhibiting more pronounced fluctuations compared with the non–spin-polarized case. The non-uniform C–C bond lengths at the defect site arise from the broken local symmetry introduced by the defect: the triangular arrangement of carbon atoms associated with the dangling bonds is inherently asymmetric, resulting in inequivalent C–C bonds. To assess whether the observed defect-induced adsorption behavior is specific to MV, additional calculations were performed for a reconstructed divacancy (5–8–5) (Fig. S7 in SI). Although the quantitative adsorption energies differ because of the distinct local atomic and electronic structures, the nature of the defect-induced perturbation remains consistent with the conclusions drawn for the MV. We further considered multilayer graphite models (without spin) in which the defect was introduced in the bottom layer (MV defect, see Fig. 4d, e, f). The results indicate that increasing the number of graphite layers beyond three leads to no significant change in the adsorption energy. In contrast, increasing the thickness from two to three layers results in an energy variation exceeding ~50 meV. While the adsorption energy increases in pristine graphite, it decreases in the defective systems, indicating that defect-induced effects extend beyond the graphene plane into the out-of-plane direction, thereby affecting the adsorption energetics (see Fig. 4e, f).

A comparison between defective and pristine graphite further shows that, beyond three layers, both systems exhibit nearly identical Li adsorption energies, differing by only a few meV. This convergence suggests that the combined effects of defects and van der Waals interactions become almost negligible with sufficient layer thickness (see Fig. 4). To further examine the spatial extent of the vacancy-induced magnetic perturbation, additional spin-polarized calculations were performed for multilayer graphite structures containing an MV in the bottom graphite layer and an adsorbed Li atom on the opposite side of the slab (see Fig. S9 in the SI). The influence of spin polarization is already small for the two-layer slab, where the Li adsorption energy differs by approximately 0.08 eV from the corresponding non-spin-polarized result. However, this difference decreases rapidly with increasing numbers of graphite layers and becomes negligible for slabs with more than three layers. These results demonstrate that the magnetic perturbation induced by the MV is rather localized and has only a negligible influence on the Li adsorption behavior of the upper graphite layers.

3.3. AM adsorption and aggregation on graphitic surfaces

The adsorption of AM atoms onto the graphite surface causes a significant transfer of electronic charge from the AM atoms to the substrate, resulting in the creation of surface dipoles. This dipole formation induces pronounced electrostatic repulsion among the adsorbed species, rendering further adsorption on the graphite surface energetically unfavorable at elevated AM concentrations. However, this dipole–dipole repulsion is only operative for separate AM adsorbates and becomes compensated through the metal–metal interaction upon the formation of adsorbed clusters. As a consequence, for higher surface coverages, the AM atoms exhibit a strong tendency to aggregate, leading to the growth of metallic clusters. The formation of these clusters is thus thermodynamically more favorable than the separate AM adsorption, facilitating the establishment of a metallic phase that avoids electrostatic repulsion. In order to study possible structures of AM clusters on graphite, the AM_xC_{400} system (with AM = Li, Na, K, and x = 1,…,9, and 15) was investigated. The formation of adsorbed AM clusters is inherently statistical and does not necessarily yield equilibrium structures. Two distinct approaches were employed to evaluate the cluster formation behavior of AM atoms on the graphite surface. In the first approach, isolated AM atoms were sequentially adsorbed onto the graphite surface in a configuration resembling a body-centered cubic (bcc) AM bulk structure, with the AM atoms positioned in up to five-layers (see Fig. 7a, and Fig. 5). The first four atoms were added, one by one, to the graphitic surface and placed adjacent to each other to form an initial cluster. Subsequently, five further atoms were deposited sequentially on top of this layer, initially occupying available bcc-like sites. Finally, to further explore cluster growth, a configuration with six additional atoms was considered, maintaining a bcc-like stacking motif. In this arrangement, one atom is positioned in the third layer, four in the fourth layer, and one in the fifth layer. It has to be noted that the configurations were always structurally optimized before the number of atoms was increased.

The obtained formation energies indicate that for both Li and Na, the cluster formation is more favorable than the single-atom adsorption. In general, after the adsorption of a few atoms, the adsorption energy approaches a plateau for the different investigated adsorbates. Notably, the considered clusters are still rather small, and only for much larger cluster sizes can the adsorption energy be expected to approach zero (i.e., the bulk value). For the case of K, there is no significant energy gain associated with the cluster formation process, however, both the single atom adsorption and the cluster formation are thermodynamically favorable with respect to the bulk metal.

In the second scenario, the AM atoms were initially distributed homogeneously in a layer at a certain distance from the surface (see Fig. 6) and then fully relaxed. Two different starting distances between the initial AM position and surface plane were investigated (≈7.0 Å and ≈3.5 Å), however, the resulting structures did not differ significantly. During the relaxation, the AM atoms are attracted by the surface, but there is also the mutual metal–metal attraction between the AMs. For low coverages (i.e., $N < 4$, which corresponds to a coverage < 2×10^{-2}), all AM atoms ended up in individual adsorption positions without any noticeable clustering. Yet, for higher coverages (N> 8, which corresponds to a coverage > 4×10^{-2}), the mutual attraction and the decreased lateral spacing between the AM atoms lead to the eventual formation of AM clusters on the graphite surface (see Fig. 7). The fluctuations that are observed in the formation energy can be attributed to the fact that not all AM atoms participate in cluster formation. Depending on the AM concentration, only a certain fraction of the AM atoms tends to aggregate, while others remain isolated on the graphite surface. At higher atomic coverage (N > 14, which corresponds to a coverage > 7×10^{-2}), where nearly all AM atoms coalesce into a cluster, the system exhibits a slightly lower adsorption energy for Li and Na as compared to the above-discussed sequential AM atom addition on bulk-like sites. For the potassium case, the energy differences are more obvious, with the single layer like distribution obtained from the homogeneous starting conditions being energetically favored. This indicates that the cluster formation for K proceeds in a different way with a preference for layer-by-layer growth. This energy reduction may arise from an optimal balance between substrate–adsorbate interactions and interatomic interactions among the AM species, resulting in enhanced stabilization and a further decrease in adsorption energy. It should be noted that for this case, some of the atoms move on top of each other while at first they were

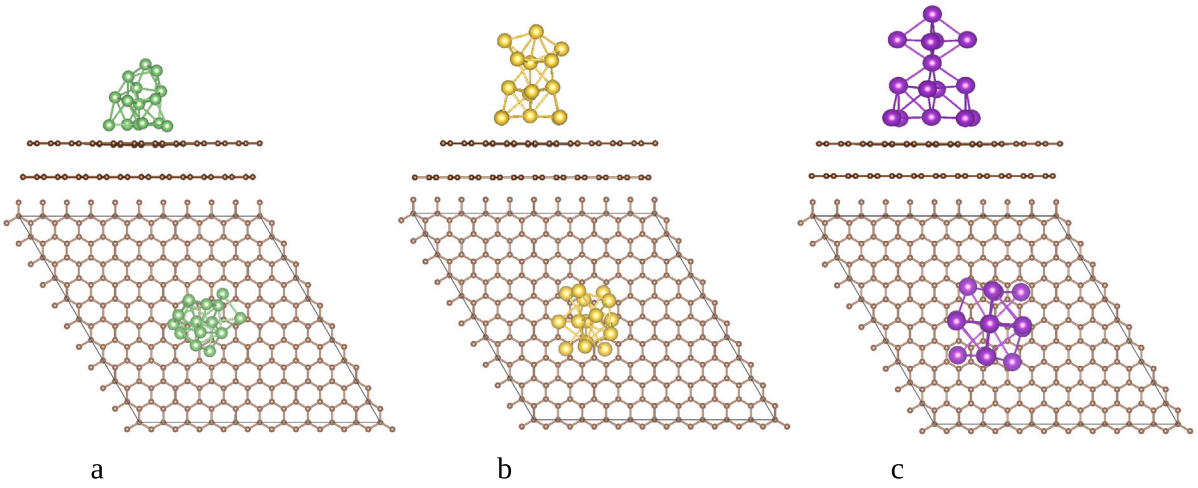

Fig. 5. Cluster formation in the $AM_{15}C_{400}$ system (AM = Li (green), Na (orange), K (purple)), mimicking the bulk AM configuration (top and side view). The structures were relaxed after AM adsorption (for more information, see also Fig. S10 in SI). (For interpretation of the references to color in this figure legend, the reader is referred to the web version of this article.)

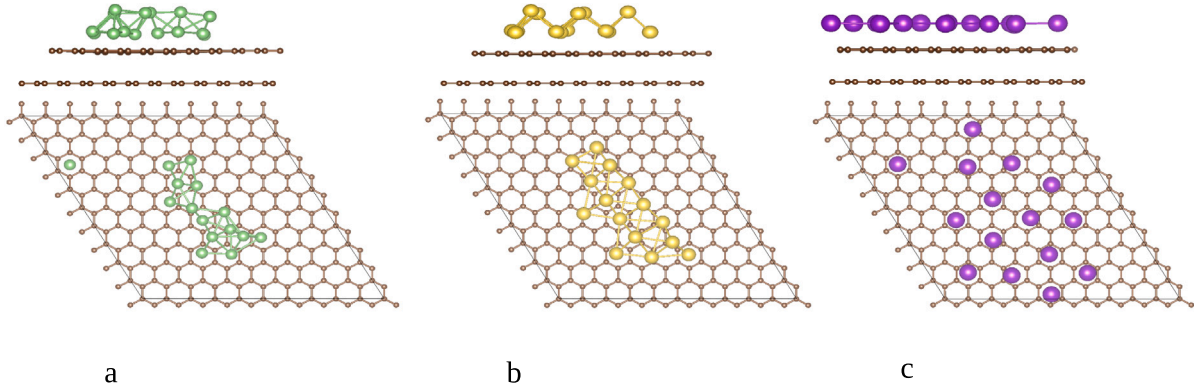

Fig. 6. Cluster formation in the $AM_{15}C_{400}$ system (AM = Li (green), Na (orange), K (purple)), starting from an initially homogeneous distribution of AM atoms (top and side view). Panels (a, b, c) correspond to structural relaxation (for more information, see also Fig. S11 and Fig. S12 in SI).

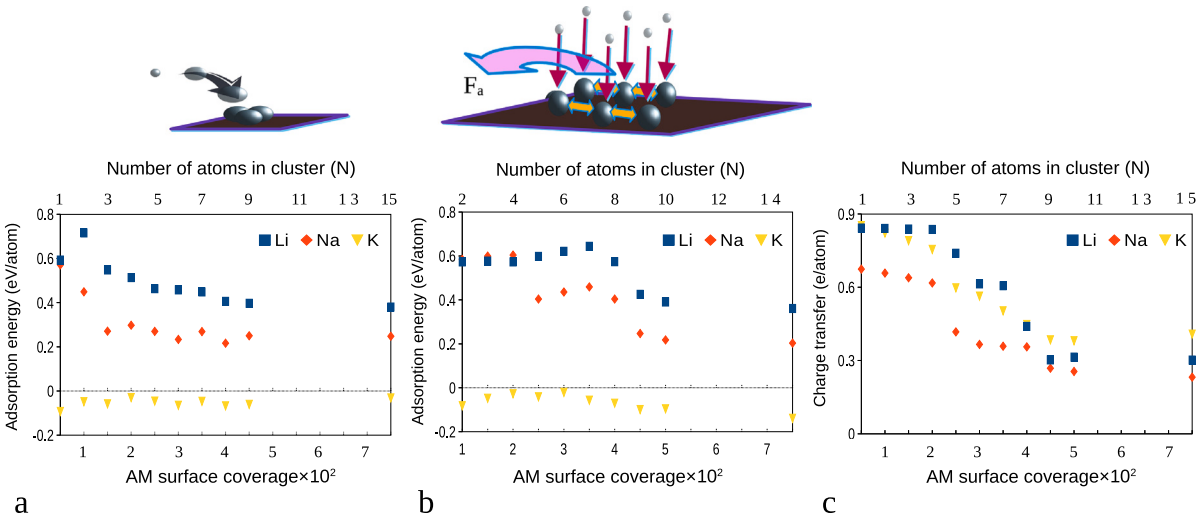

Fig. 7. Cluster formation of AM atoms on the graphite surface for two different initial scenarios. Adsorption energy per AM atom as a function of the AM surface coverage upon relaxation from (a) an initially bulk-like structure, (b) an initially homogeneously distributed flat layer ≈7.0 Å away from the surface, and (c) Average charge transferred from the AM atoms for the homogeneously distributed configuration (whole transferred charge divided by the number of AM atoms, see also Fig. S13 in SI).

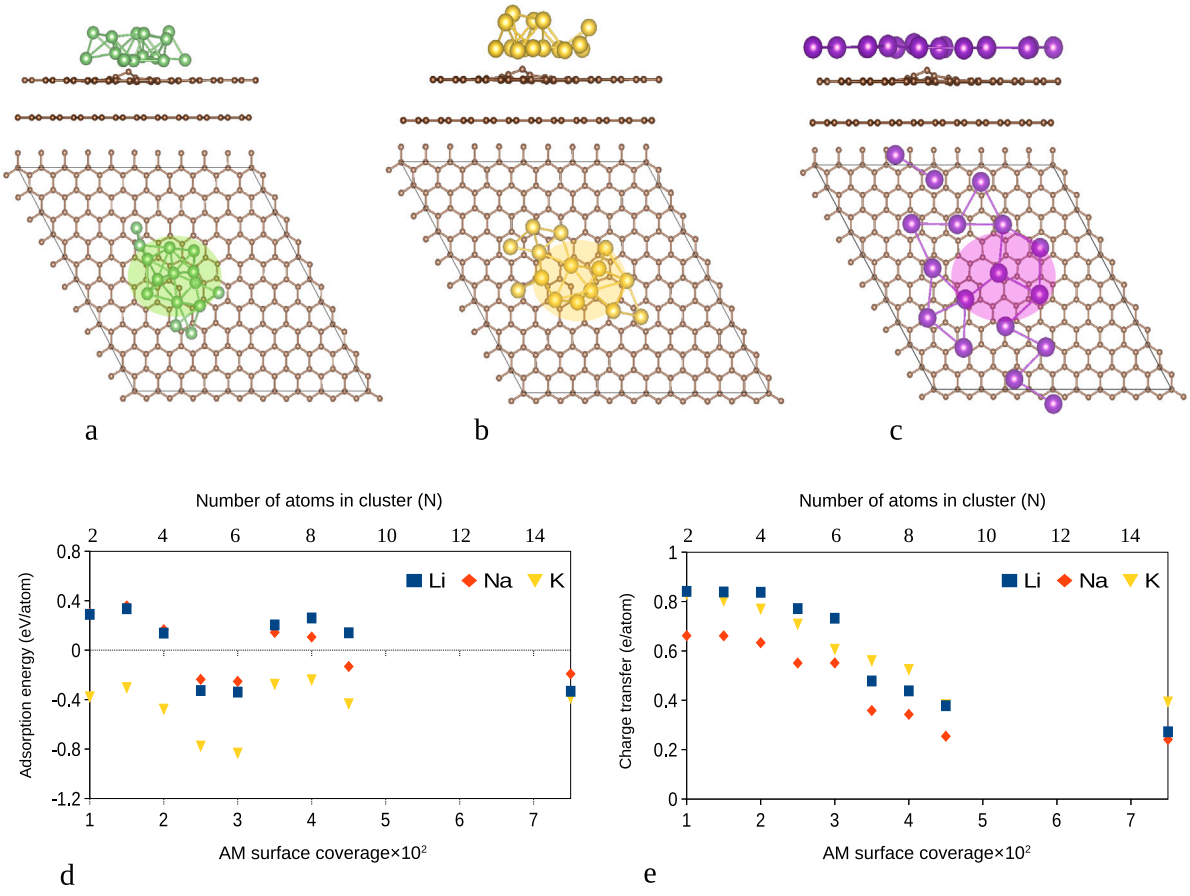

Fig. 8. AM adsorption on a graphite surface containing a monovacancy (MV) defect (side and top view). Panels (a–c) show aggregates of Li, Na, and K, respectively, with 15 AM atoms adsorbed in the vicinity of the MV defect. Panel (d) presents the adsorption energy per AM atom on the defective graphite surface, and panel (e) shows the average charge transfer upon AM adsorption as a function of the number of adsorbed AM atoms (for more information, see Fig. S14,15 in SI).

distributed at the same distance from the graphite surface as depicted in Fig. 6a, b. This finding is particularly significant, as it reveals that cluster formation on a graphite anode can occur already at the very onset of the charge process and provides a complementary perspective on clustering mechanisms besides mimicking the bcc structure. At low concentrations, the interlayer spacing close to the adsorption sites decreases slightly for the different AMs, amounting to less than 0.1 Å as compared to regions distant from the adsorbate. However, at higher concentrations, this reduction exceeds 0.1 Å, indicating that increased AM adsorption and loading induces more pronounced local lattice distortions in the graphite structure. High AM concentrations on the graphite surface, exemplified by the $AM_{15}C_{400}$ system, cause the graphite layers below the adsorbate sites to get slightly closer to each other, resulting in somewhat distorted/cavity-like domains. The energies for such distortions in the C_{400} system are found to be in the order of ≈0.1 eV for the considered AM atoms. A DDEC6 charge analysis shows that for a low AM concentration (AM_1C_{400}) of Li, Na, and K, the net charges are 0.84 e, 0.67 e, and 0.85 e, whereas for a high coverage, corresponding to $AM_{15}C_{400}$, the average charges are 0.3 e, 0.23 e, and 0.40 e, respectively (see Fig. 7c). This shows that for increasing AM concentration, the charge transfer is reduced, which lowers the electrostatic repulsion and thus favors cluster formation.

In a further approach, AIMD simulations at a finite temperature for a few configurations were performed (see Fig. S12-S14 in SI). Similar to the second scenario discussed above, the AM atoms were distributed homogeneously across the graphite surface prior to initiating the AIMD simulations at 300 K. After the AIMD simulations, the final structures were relaxed to ensure direct comparability with the previous approaches. Again, different starting distances of 7 Å and 3.5 Å above the surface were considered, yielding similar results, essentially independent of the initial distance to the surface. For the case of Li and Na, the AM atoms approach each other from the beginning, resulting in the formation of clusters on the graphite surface. It is important to note that such a cluster formation is unlikely at low coverage and low mobility, whereas the introduction of finite-temperature in the AIMD simulations enables this behavior. Notably, the cluster formation is observed even at low coverage ($N < 4$, which corresponds to a coverage $< 2 \times 10^{-2}$), hence also demonstrating a high AM mobility on the graphite surface. For the two last scenarios, relaxation and AIMD simulations of an initially homogeneous AM layer, the results turn out to be energetically rather similar, indicating the robustness of the observed trends and structures and demonstrating that AM cluster formation is favored after deposition of AM atoms on a graphite surface.

Finally, to assess the role of defects in cluster formation, we introduced a MV defect into the graphite surface (see Fig. 8). Also for this case, we employed again a homogeneous initial distribution of AM atoms across the surface to isolate the defect influence on adsorption and aggregation [74]. As in the second defect-free scenario, AM atoms were initially positioned at maximum lateral separation from one another. For AMs adsorbed rather far from the MV defect, the presence of the latter one enhances the AM adsorption energy per atom as compared to the defect-free surface for all AMs considered, even when they are initially positioned at the third- or fourth-nearest neighbor site. This indicates that, at low coverage, the adsorbates may remain spatially separated from the defect while still experiencing a significant energy gain. As the number of adsorbates increases and AM atoms get closer to the defect site, the adsorption becomes even stronger, reflecting the strong affinity of AM atoms for defective regions. Once

the defect site becomes saturated (N > 6, which corresponds to a coverage > 3×10^{-2}, see Fig. 8), the total adsorption energy begins to increase again, i.e., the total adsorption becomes weaker, until the coverage becomes sufficiently high for cluster formation to dominate (N > 7, which corresponds to a coverage > 3.5×10^{-2}). Upon the onset of this clustering, the total adsorption becomes stronger, indicating a transition to a cluster-stabilized regime. For the defect case, the adsorption energies for Li, Na, and K follow the same trend, which points to the dominant role of the defect. In particular, it has to be noticed that as soon as an AM atom is adsorbed on the defect site, this results in a significant energy gain, stabilizing the cluster formation. Again, as for the defect-free case, K tends to show a layer-like growth, while for Na and Li 3D cluster formation is observed. The corresponding charge transfer analysis reveals a progressive reduction in electron donation from the AM atoms to the graphite surface with increasing surface coverage. Li and Na exhibit a pronounced decrease beyond (N > 7, which corresponds to a coverage of 3.5×10^{-2}), while for K the change is less strong. This change corresponds to the increase in adsorption energy observed after saturation of the defect, thus also indicating a shift from charge-mediated adsorption to metallic aggregation. Moreover, it is noteworthy that the presence of a defect, even in the underlying graphite layers, significantly influences the clustering behavior on the upper surface. Our calculations demonstrate that when a defect is introduced in the bottom layer (see Fig. S15 in SI), homogeneously distributed AM atoms on the top layer tend to migrate toward the region above the defect and subsequently aggregate into a cluster. This phenomenon can be understood as the signature of the long-range influence of the defect, which affects AM adsorption not only in-plane but also through out-of-plane interactions (see Fig. 4).

4. Conclusions

The goal of this study has been to better understand the intercalation of alkali metals into the nanopores of hard carbon, which initiates via their adsorption on graphitic surfaces. Isolated adsorbed AM atoms transfer a significant amount of charge to the graphite surface, leading to the formation of surface dipoles and a pronounced dipole–dipole repulsion between individually adsorbed atoms occupying six-fold carbon rings. As a consequence of this long-range interaction, large supercells are required to obtain converged adsorption energies for single AM atoms. The presence of monovacancies results in considerably stronger adsorption, not only at the vacancy site itself but also in its vicinity, both laterally and vertically. Once AM atoms form adsorbed clusters, the adsorption energy becomes dominated by direct metal–metal interactions, yielding adsorption energies per atom that approach the cohesive energies of the corresponding alkali metals, both in the absence and presence of defects. Furthermore, Li and Na exhibit a more three-dimensional cluster growth, whereas K, due to its energetically favorable adsorption on graphite, follows a more layer-by-layer growth mechanism. Overall, our results provide a consistent and physically grounded picture of alkali-metal cluster formation in graphitic materials such as hard carbon, particularly under conditions of increased AM concentration and surface coverage. By explicitly accounting for long-range interatomic interactions, coverage-dependent effects, and the influence of defects, we establish a comprehensive description of alkali-metal adsorption energetics and clustering mechanisms. The excellent agreement among the sequential adsorption calculations, homogeneous initial configurations, ab initio molecular dynamics simulations, DDEC6 charge-transfer analysis, estimated interface dipoles, and electrostatic potential calculations provides a consistent physical picture demonstrating that long-range electrostatic interactions govern the coverage-dependent adsorption and clustering behavior of alkali metals on graphitic surfaces. These findings provide deeper insight into the mechanisms governing cluster formation and their implications for the electrochemical performance of carbon-based anode materials.

CRediT authorship contribution statement

Jafar Azizi: Writing – review & editing, Writing – original draft, Formal analysis, Data curation, Conceptualization. **Axel Gross:** Writing – review & editing, Supervision. **Holger Euchner:** Writing – review & editing, Validation, Supervision.

Declaration of competing interest

The authors declare that they have no known competing financial interests or personal relationships that could have appeared to influence the work reported in this paper.

Acknowledgments

This work contributes to research performed at CELEST (Center for Electrochemical Energy Storage Ulm–Karlsruhe) and was funded by the German Research Foundation (DFG) under Project ID 390874152 (POLiS Cluster of Excellence). The authors acknowledge computational support from the state of Baden-Württemberg through bwHPC, the DFG through grant no. INST 40/575-1 FUGG (JUSTUS 2 cluster), and the HoreKa supercomputer funded by the Ministry of Science, Research and the Arts Baden-Württemberg and the Federal Ministry of Education and Research. Further support from the Dr. Barbara Mez-Starck Foundation is gratefully acknowledged.

Appendix A. Supplementary information

Supplementary material related to this article can be found online at https://doi.org/10.1016/j.jpowsour.2026.241282.Additional results and figures are given in the Supporting Information file (SI).

The data that support the findings of this study are available via the Zenodo repository https://doi.org/10.5281/zenodo.22205946.

Data availability

The data that support the findings of this study are available via the Zenodo repository.

References

[1] E. Dokur, S. Uruc, R. Kurteli, O. Gorduk, Y. Sahin, Investigation of flexible electrochemical sensor properties of graphite conductive ink modified textile products and their applications in electrical circuits, Mater. Today Commun. 37 (2023) 106920.
[2] P. Murugan, R.D. Nagarajan, B.H. Shetty, M. Govindasamy, A.K. Sundramoorthy, Recent trends in the applications of thermally expanded graphite for energy storage and sensors–a review, Nanoscale Adv. 3 (22) (2021) 6294–6309.
[3] R.L. McCreery, Advanced carbon electrode materials for molecular electrochemistry, Chem. Rev. 108 (7) (2008) 2646–2687.
[4] M. Pumera, The electrochemistry of carbon nanotubes: fundamentals and applications, Chem. Eur. J. 15 (20) (2009) 4970–4978.
[5] Y.-F. Li, M.-Q. Guo, S.-F. Yin, L. Chen, Y.-B. Zhou, R.-H. Qiu, C.-T. Au, Graphite as a highly efficient and stable catalyst for the production of lactones, Carbon 55 (2013) 269–275.
[6] L.R. Radovic, F. Rodriguez-Reinoso, Carbon materials in catalysis, Chem. Phys. Carbon (1996) 261–376.
[7] P. Serp, B. Machado, Nanostructured Carbon Materials for Catalysis, (23) Royal Society of Chemistry, 2015.
[8] A. Carlos, D.L. y Leon, L.R. Radovic, Interfacial chemistry and electrochemistry of carbon surfaces, Chem. Phys. Carbon (2023) 213–310.
[9] A. Jänes, H. Kurig, E. Lust, Characterisation of activated nanoporous carbon for supercapacitor electrode materials, Carbon 45 (6) (2007) 1226–1233.
[10] T. Kesavan, T. Partheeban, M. Vivekanantha, M. Kundu, G. Maduraiveeran, M. Sasidharan, Hierarchical nanoporous activated carbon as potential electrode materials for high performance electrochemical supercapacitor, Microporous Mesoporous Mater. 274 (2019) 236–244.
[11] J. Huang, B.G. Sumpter, V. Meunier, A universal model for nanoporous carbon supercapacitors applicable to diverse pore regimes, carbon materials, and electrolytes, Chem. Eur. J. 14 (22) (2008) 6614–6626.

[12] D. Deng, Li-ion batteries: basics, progress, and challenges, Energy Sci. Eng. 3 (5) (2015) 385–418.
[13] V. Etacheri, R. Marom, R. Elazari, G. Salitra, D. Aurbach, Challenges in the development of advanced Li-ion batteries: a review, Energy Environ. Sci. 4 (9) (2011) 3243–3262.
[14] A. Urban, D.-H. Seo, G. Ceder, Computational understanding of Li-ion batteries, Npj Comput. Mater. 2 (1) (2016) 1–13.
[15] J. Azizi, A. Groß, H. Euchner, Unveiling the potential of lignin-derived hard carbon as an anode material for Li- and post-Li-ion batteries: a computational investigation, "J. Mater. Chem. A" (2026) http://dx.doi.org/10.1039/D6TA00336B, Advance Article.
[16] J. Azizi, A. Groß, H. Euchner, Tailoring adsorption properties of graphitic surfaces: Toward improved anode materials for Li-and post-Li ion batteries, Batteries & Supercaps 9 (1) (2026) e202500382.
[17] L.-F. Zhao, Z. Hu, W.-H. Lai, Y. Tao, J. Peng, Z.-C. Miao, Y.-X. Wang, S.-L. Chou, H.-K. Liu, S.-X. Dou, Hard carbon anodes: fundamental understanding and commercial perspectives for na-ion batteries beyond li-ion and K-ion counterparts, Adv. Energy Mater. 11 (1) (2021) 2002704.
[18] S. Komaba, W. Murata, T. Ishikawa, N. Yabuuchi, T. Ozeki, T. Nakayama, A. Ogata, K. Gotoh, K. Fujiwara, Electrochemical Na insertion and solid electrolyte interphase for hard-carbon electrodes and application to Na-Ion batteries, Adv. Funct. Mater. 21 (20) (2011) 3859–3867.
[19] Z. Li, Y. Chen, Z. Jian, H. Jiang, J.J. Razink, W.F. Stickle, J.C. Neuefeind, X. Ji, Defective hard carbon anode for Na-ion batteries, Chem. Mater. 30 (14) (2018) 4536–4542.
[20] D. Aurbach, B. Markovsky, I. Weissman, E. Levi, Y. Ein-Eli, On the correlation between surface chemistry and performance of graphite negative electrodes for Li ion batteries, Electrochim. Acta 45 (1–2) (1999) 67–86.
[21] A. Senyshyn, M. Mühlbauer, O. Dolotko, H. Ehrenberg, Low-temperature performance of Li-ion batteries: The behavior of lithiated graphite, J. Power Sources 282 (2015) 235–240.
[22] C. Mao, M. Wood, L. David, S.J. An, Y. Sheng, Z. Du, H.M. Meyer, R.E. Ruther, D.L. Wood, Selecting the best graphite for long-life, high-energy Li-ion batteries, J. Electrochem. Soc. 165 (9) (2018) A1837.
[23] J. Azizi, A. Groß, H. Euchner, Uncovering the early-stage intercalation mechanism in graphite-based anode materials, ACS Appl. Mater. Interfaces 17 (2025) 33965.
[24] J. Azizi, A. Groß, H. Euchner, Computational investigation of carbon based anode materials for Li-and Post-Li-Ion batteries, ChemSusChem 17 (14) (2024) e202301493.
[25] M. Jäckle, K. Helmbrecht, M. Smits, D. Stottmeister, A. Groß, Self-diffusion barriers: possible descriptors for dendrite growth in batteries? "Energy Env. Sci." 11 (2018) 3400–3407, http://dx.doi.org/10.1039/C8EE01448E.
[26] S.K. Saju, S. Chattopadhyay, J. Xu, S. Alhashim, A. Pramanik, P.M. Ajayan, Hard carbon anode for lithium-, sodium-, and potassium-ion batteries: Advancement and future perspective, Cell Rep. Phys. Sci. 5 (3) (2024) 398–402.
[27] H. Zheng, Q. Qu, L. Zhang, G. Liu, V.S. Battaglia, Hard carbon: a promising lithium-ion battery anode for high temperature applications with ionic electrolyte, RSC Adv. 2 (11) (2012) 4904–4912.
[28] D. Stevens, J. Dahn, High capacity anode materials for rechargable sodium-ion batteries, J. Electrochem. Soc. 147 (2000) 1271.
[29] M. Anji Reddy, M. Helen, A. Groß, M. Fichtner, H. Euchner, Insight into sodium insertion and the storage mechanism in hard carbon, ACS Energy Lett. 3 (12) (2018) 2851–2857.
[30] H. Euchner, B. Vinajan, M. Anji Reddy, M. Fichtner, A. Groß, Alkali metal insertion in hard carbon – the full picture, J. Mater. Chem. A 8 (2020) 14205.
[31] D. Li, Two-dimensional c 5678: A promising carbon-based high-performance lithium-ion battery anode, Mater. Adv. 2 (1) (2021) 398–402.
[32] Y. Li, Y. Lu, P. Adelhelm, M.-M. Titirici, Y.-S. Hu, Intercalation chemistry of graphite: alkali metal ions and beyond, Chem. Soc. Rev. 48 (17) (2019) 4655–4687.
[33] M. Johnson, H. Starnberg, H. Hughes, Electronic structure of alkali metal overlayers on graphite, Surf. Sci. 178 (1–3) (1986) 290–299.
[34] M. Caragiu, S. Finberg, Alkali metal adsorption on graphite: a review, J. Phys.: Condens. Matter. 17 (35) (2005) R995.
[35] H. Euchner, A. Groß, Atomistic modeling of Li- and post-Li-ion batteries, Phys. Rev. Mater. 6 (2022) 040302, http://dx.doi.org/10.1103/PhysRevMaterials.6.040302.
[36] A. Srinivas, A. Dash, S.C.B. Jakka, DFT-MD simulations and experimental validation of graphene-CO_2 interaction energies and structural dynamics for enhanced CO_2 adsorption, Next Mater. 8 (2025) 100912.
[37] J. Van De Streek, M.A. Neumann, Validation of experimental molecular crystal structures with dispersion-corrected density functional theory calculations, Struct. Sci. 66 (5) (2010) 544–558.
[38] M. Jaraiz, L. Enriquez, R. Pinacho, J.E. Rubio, A. Lesarri, J.L. Lopez-Perez, A DFT-based computational-experimental methodology for synthetic chemistry: Example of application to the catalytic opening of epoxides by titanocene, J. Org. Chem. 82 (7) (2017) 3760–3766.
[39] K. Hemelsoet, F. De Vleeschouwer, V. Van Speybroeck, F. De Proft, P. Geerlings, M. Waroquier, Validation of DFT-based methods for predicting qualitative thermochemistry of large polyaromatics, ChemPhysChem 12 (6) (2011) 1100–1108.
[40] E.O. Gomes, G.S. Fabris, M.M. Ferrer, F.V. Motta, M.R. Bomio, J. Andres, E. Longo, J.R. Sambrano, Computational procedure to an accurate DFT simulation to solid state systems, Comput. Mater. Sci. 170 (2019) 109176.
[41] S. Kirklin, J.E. Saal, B. Meredig, A. Thompson, J.W. Doak, M. Aykol, S. Rühl, C. Wolverton, The open quantum materials database (OQMD): assessing the accuracy of DFT formation energies, Npj Comput. Mater. 1 (1) (2015) 1–15.
[42] E. Yoo, J. Kim, E. Hosono, H.-s. Zhou, T. Kudo, I. Honma, Large reversible li storage of graphene nanosheet families for use in rechargeable lithium ion batteries, Nano Lett. 8 (8) (2008) 2277–2282.
[43] W.-Q. Deng, X. Xu, W.A. Goddard, New alkali doped pillared carbon materials designed to achieve practical reversible hydrogen storage for transportation, Phys. Rev. Lett. 92 (16) (2004) 166103.
[44] G. Zhao, X. Li, M. Huang, Z. Zhen, Y. Zhong, Q. Chen, X. Zhao, Y. He, R. Hu, T. Yang, et al., The physics and chemistry of graphene-on-surfaces, Chem. Soc. Rev. 46 (15) (2017) 4417–4449.
[45] A.V. Verkhovtsev, Y. Erofeev, A.V. Solov'yov, Soft landing of metal clusters on graphite: a molecular dynamics study, Eur. Phys. J. D 74 (10) (2020) 205.
[46] Z. Li, K. Hock, R. Palmer, J. Annett, Potassium-adsorption-induced plasmon frequency shift in graphite, J. Phys.: Condens. Matter. 3 (S) (1991) S103.
[47] A. Sandell, O. Hjortstam, A. Nilsson, P. Brühwiler, O. Eriksson, P. Bennich, P. Rudolf, J. Wills, B. Johansson, N. Mårtensson, Bonding of an isolated k atom to a surface: Experiment and theory, Phys. Rev. Lett. 78 (26) (1997) 4994.
[48] K. Rytkönen, J. Akola, M. Manninen, Density functional study of alkali-metal atoms and monolayers on graphite (0001), Phys. Rev. B—Condensed Matter Mater. Phys. 75 (7) (2007) 075401.
[49] X. Liu, C. Wang, Y. Yao, W. Lu, M. Hupalo, M. Tringides, K. Ho, Bonding and charge transfer by metal adatom adsorption on graphene, Phys. Rev. B—Condensed Matter Mater. Phys. 83 (23) (2011) 235411.
[50] K.T. Chan, J. Neaton, M.L. Cohen, First-principles study of metal adatom adsorption on graphene, Phys. Rev. B—Condensed Matter Mater. Phys. 77 (23) (2008) 235430.
[51] J. Jiao, R. Xiao, M. Tian, Z. Wang, L. Chen, First-principles calculations on lithium and sodium adsorption on graphene edges, Electrochim. Acta 282 (2018) 205–212.
[52] X. Zhang, M. Ghorbani-Asl, Y. Zhang, A.V. Krasheninnikov, Quasi-2D FCC lithium crystals inside defective bi-layer graphene: insights from first-principles calculations, Mater. Today Energy 34 (2023) 101293.
[53] J. Barnard, K. Hock, R. Palmer, Intercalation of potassium from the surface of graphite, Surf. Sci. 287 (1993) 178–182.
[54] Z. Li, K. Hock, R. Palmer, Phase transitions and excitation spectrum of submonolayer potassium on graphite, Phys. Rev. Lett. 67 (12) (1991) 1562.
[55] K. Hock, R. Palmer, Temperature dependent behaviour in the adsorption of submonolayer potassium on graphite, Surf. Sci. 284 (3) (1993) 349–360.
[56] H. Guo, Y. Tian, Y. Liu, Y. Bai, J. Wu, F. Kang, B. Li, Inner lithium fluoride (LiF)-rich solid electrolyte interphase enabled by a smaller solvation sheath for fast-charging lithium batteries, ACS Appl. Mater. Interfaces 15 (1) (2022) 1201–1209.
[57] X. Qi, H.-B. Zhang, J. Xu, X. Wu, D. Yang, J. Qu, Z.-Z. Yu, Highly efficient high-pressure homogenization approach for scalable production of high-quality graphene sheets and sandwich-structured α-Fe2O3/graphene hybrids for high-performance lithium-ion batteries, ACS Appl. Mater. Interfaces 9 (12) (2017) 11025–11034.
[58] M. Julia, J. Fabian, B. Daniel, E. Kristina, V. Mario, Surface layer evolution on graphite during electrochemical sodium-tetraglyme Co-intercalation, ACS Appl. Mater. Interfaces 9 (14) (2017) 12373–12381.
[59] G. Kresse, J. Furthmüller, Efficient iterative schemes for ab initio total-energy calculations using a plane-wave basis set, Phys. Rev. B 54 (16) (1996) 11169.
[60] M. Dion, H. Rydberg, E. Schröder, D.C. Langreth, B.I. Lundqvist, Van der waals density functional for general geometries, Phys. Rev. Lett. 92 (24) (2004) 246401.
[61] J.P. Perdew, Generalized gradient approximation made simple, Phys. Rev. Lett. 77 (1997) 3868.
[62] S. Grimme, Semiempirical GGA-type density functional constructed with a long-range dispersion correction, J. Comput. Chem. 27 (15) (2006) 1787–1799.
[63] S. Grimme, S. Ehrlich, L. Goerigk, Effect of the damping function in dispersion corrected density functional theory, J. Comput. Chem. 32 (7) (2011) 1456–1465.
[64] J.I. Martinez, I. Cabria, M. López, J. Alonso, Adsorption of lithium on finite graphitic clusters, J. Phys. Chem. C 113 (3) (2009) 939–941.
[65] N. Dimakis, I. Salas, L. Gonzalez, O. Vadodaria, K. Ruiz, M.I. Bhatti, Li and Na adsorption on graphene and graphene oxide examined by density functional theory, quantum theory of atoms in molecules, and electron localization function, Molecules 24 (4) (2019) 754.
[66] E. Lee, K.A. Persson, Li absorption and intercalation in single layer graphene and few layer graphene by first principles, Nano Lett. 12 (9) (2012) 4624–4628.

[67] F. Gossenberger, T. Roman, A. Groß, Hydrogen and halide co-adsorption on Pt(111) in an electrochemical environment: a computational perspective, "Electrochim. Acta" 216 (2016) 152–159, http://dx.doi.org/10.1016/j.electacta.2016.08.117.

[68] T.A. Manz, N.G. Limas, Introducing DDEC6 atomic population analysis: part 1. Charge partitioning theory and methodology, RSC Adv. 6 (53) (2016) 47771–47801.

[69] N.G. Limas, T.A. Manz, Introducing DDEC6 atomic population analysis: part 2. Computed results for a wide range of periodic and nonperiodic materials, RSC Adv. 6 (51) (2016) 45727–45747.

[70] H. Kim, J.-M. Choi, W.A. Goddard III, Universal correction of density functional theory to include London dispersion (up to Lr, element 103), J. Phys. Chem. Lett. 3 (3) (2012) 360–363.

[71] P.O. Lehtinen, A.S. Foster, Y. Ma, A. Krasheninnikov, R.M. Nieminen, Irradiation-induced magnetism in graphite: a density functional study, Phys. Rev. Lett. 93 (18) (2004) 187202.

[72] Y. Zhang, S. Talapatra, S. Kar, R. Vajtai, S. Nayak, P. Ajayan, First-principles study of defect-induced magnetism in carbon, Phys. Rev. Lett. 99 (10) (2007) 107201.

[73] X. Yang, H. Xia, X. Qin, W. Li, Y. Dai, X. Liu, M. Zhao, Y. Xia, S. Yan, B. Wang, Correlation between the vacancy defects and ferromagnetism in graphite, Carbon 47 (5) (2009) 1399–1406.

[74] J. Cottom, Q. Cai, E. Olsson, Vacancy enhanced li, na, and k clustering on graphene, Sustain. Energy Fuels 9 (10) (2025) 2813–2826.